International Journal of Modern Physics B Vol. 28 (2014) 1430018 (27 pages) © World Scientific Publishing Company DOI: 10.1142/S0217979214300187



# Development of nonlinear optical materials promoted by density functional theory simulations

Xingxing Jiang\*,‡, Lei Kang\*,‡, Siyang Luo\*, Pifu Gong\*,‡, Ming-Hsien Lee†,§, $\parallel$  and Zheshuai Lin\*,¶, $\parallel$ 

\*Beijing Center for Crystal R&D, Key Laboratory of Functional Crystals and Laser Technology of the Chinese Academy of Sciences,

Technical Institute of Physics and Chemistry, Chinese Academy of Sciences,

Beijing 100190, P. R. China

†Department of Physics, Tamkang University, Tamsui,

New Taipei 25137, Taiwan

‡University of the Chinese Academy of Sciences,

Beijing 100049, P. R. China

§mhslee@mail.tku.edu.tw

¶zslin@mail.ipc.ac.cn

Received 27 September 2014 Accepted 6 October 2014 Published 30 October 2014

Nonlinear optical (NLO) crystals are very important optoelectronic functional materials and their developments have significantly contributed to the progress of laser science and technology for decades. In order to explore new NLO crystals with superior performances, it is greatly desirable to understand the intrinsic relationship between the macroscopic optical properties and microscopic structural features in crystals. In this paper, the applications of density functional theory (DFT) method to the elucidation of the structure-property relationship and to the exploration on novel NLO materials in the ultraviolet and infrared spectrum regions are reviewed. The great success in the linear and NLO property predictions has been achieved using the first-principles computational simulations, and the mechanism understanding obtained by various analysis tools can give substantial guidance to the search and design of new NLO crystals.

Keywords: First-principles; nonlinear optical property; structure-property relationship.

PACS numbers: 42.70.Mp, 71.20.Ps, 82.20.Wt

#### 1. Introduction

In 1960, Maiman invented the first laser,<sup>1</sup> and shortly in 1961, Franklin observed the second harmonic generation (SHG) phenomenon in silicon dioxide.<sup>2</sup> Since then, stimulated by the rapid development of lasers, the nonlinear optics has become

Corresponding author.

an increasingly attractive research field and largely promoted the progress of laser science and technology in return.<sup>3-12</sup> In the nonlinear optical (NLO) processes, the NLO crystals play the vital role to broaden the spectral ranges of the laser to ultraviolet (UV), infrared (IR) and even Tera-Hz regions. The lasers in these regions are very useful for the industrial technology and scientific research, for example, the UV laser shows much advantage in ultrafine micro-manufacture and high-precision spectral analysis, and the IR laser exhibits wide application potentials in remote sensing and optical communications. Therefore, the NLO crystals with superior performances described below in these spectral regions are urgently demanded.

In order to effectively generate the coherent laser radiation in the UV region, the optical properties of a NLO crystal needs to satisfy some criterions.<sup>13</sup> Firstly, the crystals must possess a large energy band gap  $(E_g)$  to guarantee the optical transmission in UV region. Secondly, the SHG coefficient  $(d_{ij})$  of the crystal must be large as possible, typically should be larger than  $1 \times \text{KDP}(0.39 \text{ pm/V})$ , so as to obtain the high conversion efficiency. Thirdly, the crystal must have an appropriate birefringence  $(\Delta n = n_{\text{max}}(\lambda) - n_{\text{min}}(\lambda))$  to achieve the phase-matching condition for SHG, where the  $n_{\text{max}}(\lambda)$  and  $n_{\text{min}}(\lambda)$  are the largest and smallest refractive index at the wavelength  $\lambda$ , respectively. In general, the birefringence for a UV NLO crystal should be larger than 0.060 and this value should be larger (e.g., > 0.075) for the deep-UV NLO crystals due to the steeper dispersion of refractive indices for the higher photon energy. However, too large birefringence is not good either, because it would result in the walk-off and self-focus effect which can reduce the conversion efficiency and damage the sample, respectively.

The requirements of optical performance for the IR NLO crystals are different. Compared with UV region, the dispersive curve of crystal in IR region is flat, so generally the birefringence about 0.03 is enough to obtain the IR coherent wave generation by a NLO crystal. Meanwhile, in order to achieve the same conversion efficiency as in the UV region, the SHG effect in IR NLO crystal should be larger than  $10 \times \text{KDP}$ , since the efficiency is proportional to the  $d_{ij}/\lambda$ . Another important optical parameter for the practical applications of IR NLO crystal is the laser damage threshold (LDT). Typically, the LDT value larger than 100 MW/cm² for a nanosecond laser is enough for almost all academic and commercial purposes in the current stage. Because the strong positive correlation exists between the LDT and energy band gap in a crystal (LDT  $\sim 100 \text{ MW/cm}^2$  corresponding to  $E_g \sim 3.0 \text{ eV}$ ), the crystals with large LDT should possess wide energy band gap. However, the increase of energy band gap usually results in the decrease of the NLO response in crystals. Therefore, it is a very important issue to achieve the balance between energy band gap and SHG effect for the explorations on good IR NLO crystals.  $^{14}$ 

A thorough elucidation of the structure–properties relationship between the micro-structure and NLO performance has significant implications to the search and design of new NLO crystals. Indeed the discovery of a crystal with good NLO performance in tens thousands of materials just by "trial and error" method is a very huge task. The in-depth understandings of the mechanism how the struc-

ture determines the NLO behavior would provide the research direction for the experimental explorations, and save enormous human and material resources. In the history of development of NLO crystals, a few theoretical models have been proposed such as Miller's rule, <sup>15</sup> anharmonic oscillator models, <sup>16</sup> the bond parameter and charge model, <sup>17</sup> charge transfer model, <sup>18</sup> and anionic group theory. <sup>19</sup> These models have successfully elaborated the structure–properties relationship in specific type of materials and greatly promoted the research of NLO crystals. However, in these methods the experimental data are inevitably introduced, so heavily affect the predicting capability of the empirical or semi-empirical models.

Thanks to the rapid development of computational method and supercomputer facilities, the first-principles methods, especially the density functional theory (DFT) based, have been applied to the research of NLO materials since the end of 1990s. The NLO coefficients, energy band gaps, refractive indices and birefringence can be calculated and predicted without any experimental data. More importantly, some computational tools have been developed to analyze the microscopic mechanism of the linear and NLO properties in UV and IR NLO crystals.<sup>20</sup> These studies have made significant contributions to the search and design of NLO crystals from the atomic scale.

In this review, our studies on the NLO crystals by the first-principles method are reviewed. In Sec. 2, the introduction of computational method based on DFT and the developed analysis tools are presented. In Secs. 3 and 4, the application of the first-principles method to the prediction and design of UV and IR crystals are introduced, respectively. Finally, the prospects of the first-principles method in the research of NLO crystals are proposed.

### 2. First-Principles Research Methods

## 2.1. Computational methods on optical properties based on DFT

To the present day, DFT is the most efficient method to determine the electronic ground states and has been successfully used to predict the various properties of the materials. <sup>21,22</sup> However, the optical properties of materials are closely related to the electronic excitation. <sup>23</sup> The energy band gap prediction is a very difficult task for DFT because the exact exchange–correlation functionals are unknown: in local density approximation (LDA)<sup>24</sup> and general gradient approximation (GGA)<sup>25</sup> the predicted energy band gaps are always smaller than the experimental values, typically by around 40% for the wide-gap insulators. In recent years quite a few exchange-correlation functionals beyond LDA and GGA have been developed, such as HF (exact exchange, but no correlation), HF-LDA (exact-exchange, plus LDA correction), sX (screened exchange, but no correlation), and sX-LDA (screened exchange, plus LDA correlation) forms, <sup>26</sup> hybrid functionals with B3LYP (combination of HF exchange with DFT XC)<sup>27</sup> and PBE0 (combination of PBE functional with a predefined amount of exact exchange) forms. <sup>28</sup> Our tests have shown that for the UV and deep-UV crystals the energy band gaps predicted by the hybridized

functional PBE0 and B3LYP show good agreement with measured values and the calculated error are usually less than 5%, while for the IR crystals of semiconductor type the data obtained by sX-LDA functionals usually give satisfactory results.<sup>29</sup> Thus, electronic band structure (both energy band gaps and electronic band dispersion) can be well reproduced by first-principles calculation in true sense and the optical properties can be predicted totally independent from the experimental data.

Our electric structure calculations were performed by CASTEP,<sup>30</sup> a total energy DFT package based on plane-wave pseudopotential method. The  $q_c$ -tunning<sup>31</sup> optimized<sup>32,33</sup> norm-conserving pseudopotentials in the Kleinman–Bylander form<sup>34</sup> were adopted to model the interaction between the valence electrons and ion cores, which allow us choose a relatively small plane-wave basis set without compromising the accuracy. Kinetic energy cutoff of 900 eV and Monkhorst–Pack k-point meshes<sup>35</sup> spanning less than 0.04 Å<sup>-3</sup> separation in the Brillouin zones were typically chosen. For the optical properties calculations, the number of electronic states in the conduction band (CB) was chosen as three times of the number in the valence band (VB). The convergence test revealed that the above computational parameters are sufficiently accurate for the study of NLO properties.

Based on the obtained electric structures, the imaginary part of the dielectric function  $\varepsilon_2$  can be calculated from the electronic transition across the band gap caused by the interaction with photons, using the formula,<sup>36</sup>

$$\varepsilon_2(\hbar\omega) = \frac{2\pi e^2}{\Omega\varepsilon_0} \sum_{k,v,c} |\langle \Psi_k^c | \hat{u} \cdot \mathbf{r} | \Psi_k^v \rangle|^2 \delta(E_k^c - E_k^v - \hbar\omega). \tag{1}$$

Here  $\Omega$  is the volume of the unit cell and v and c represent the valence and conduction bands, respectively.  $\omega$  and  $\hat{u}$  represent the frequency and the unit vector in the polarization direction of the incident light. Under periodic boundary condition,  $|\langle \Psi_k^c | \hat{u} \cdot \mathbf{r} | \Psi_k^v \rangle|$  is the transition matrix element between a VB and a CB at a specific k point in the first Brillouin zone. By Kramers–Kronig transform, the real part of the dielectric function can be obtained from the imaginary part, and then the theoretical refractive index n and birefringence  $\Delta n$  can be determined.

Without considering the dispersive effect, the NLO response in a crystal can be evaluated by the static limit of the SHG coefficient  $\chi^{(2)}$ . We implemented the formula proposed by Rashkeev<sup>37</sup> to calculate the static SHG coefficient, which is expressed as<sup>38</sup>:

$$\chi^{ijk} = \chi^{ijk}(VE) + \chi^{ijk}(VH) + \chi^{ijk}(twobands), \qquad (2)$$

where  $\chi^{ijk}$  (VE) and  $\chi^{ijk}$  (VH) are the contribution of the virtual electron and virtual hole process, respectively, and  $\chi^{ijk}$  (two bands) is the contribution of the two bands process. The exact expressions for the three terms are presented as follows:

$$\chi^{ijk}(VE) = \frac{e^3}{2\hbar^2 m^3} \sum_{vcc'} \int \frac{d^3 \mathbf{k}}{4\pi^3} P(ijk) \text{Im}[p_{vc}^i p_{cc'}^j p_{c'v}^k] \left(\frac{1}{\omega_{cv}^3 \omega_{vc'}^2} + \frac{2}{\omega_{vc}^4 \omega_{c'v}}\right), \quad (3)$$

$$\chi^{ijk}(VH) = \frac{e^3}{2\hbar^2 m^3} \sum_{vv'c} \int \frac{d^3 \mathbf{k}}{4\pi^3} P(ijk) \text{Im}[p^i_{vv'} p^j_{v'c} p^k_{cv}] \left( \frac{1}{\omega^3_{cv} \omega^2_{v'c}} + \frac{2}{\omega^4_{vc} \omega_{cv'}} \right), \quad (4)$$

$$\chi^{ijk}(\text{twobands}) = \frac{e^3}{\hbar^2 m^3} \sum_{vc} \int \frac{d^3 \mathbf{k}}{4\pi^3} P(ijk) \frac{\text{Im}[p_{vc}^i p_{cv}^j (p_{vv}^k - p_{cc}^k)]}{\omega_{vc}^5},$$
 (5)

where i,j,k denote the Cartesian component, v and v' represent VBs and c and c' represent the CBs. P(ijk) denotes the full permutation.  $\hbar\omega_{mn}$  and  $p_{mn}^{\alpha}$  are the energy difference and momentum matrix element between the electronic states m and n of the same k-point ( $\mathbf{k}$ ) which is not labeled for simplicity. Usually, the  $\chi^{ijk}$  is simplified to  $d_{il}$  by a factor 1/2 (i.e.,  $d_{il}=1/2\chi^{ijk}$ ) with the transformation relationship:  $11 \to 1$ ;  $22 \to 2$ ;  $33 \to 3$ ; 23,  $32 \to 4$ ; 13,  $31 \to 5$  and 12,  $21 \to 6$ . Thus, the linear and NLO properties can be well determined by the above formula deduced from the first- and second-order perturbations on the ground electronic states, respectively, because intrinsically these optical properties are determined by the virtual electronic excitation processes.

## 2.2. The mechanism analysis tools

The accurately predicted optical properties provide us much confidence of the application of DFT to NLO properties. Accordingly, with the purpose to searching and designing for novel NLO crystals, we developed several useful tools to deeply investigate the structure–property relationship in NLO crystals, including the real space atom cutting technique<sup>38</sup> and SHG density.<sup>39–41</sup>

#### 2.2.1. Real space atom cutting technique

The real space atom cutting technique was developed to analyze the contribution of respective ions or ionic groups to the overall optical properties. In this method, the whole real space of the crystal cell is partitioned into several union of individual sphere zones to the respective ions (groups). The sphere zones separated to the ions is mainly determined by the radius of the ions (the radii of the atoms contained in the groups) following the rule that the spheres should not be overlapping with each other. Regarding the contribution to the optical properties from a specific ion (or group), the wavefunction in the zones belonging to the other ions (groups) is set to zero (referred as "atom cutting") and band-to-band transition (momentum) matrix elements re-evaluated for a further polarizability calculation. The contribution of focusing ion (group) to the nth polarizability is

$$\chi^n(X) = \chi^n(\text{all the atoms are cutting except } X)$$
. (6)

#### 2.2.2. SHG density analysis

By real space atom cutting technique, the contribution of respective ions and groups can be quantitatively extracted. In order to more intuitively display the contribution of electronic orbitals to the SHG effect, we developed the SHG-weighted charge density analysis scheme.<sup>39–41</sup> In this methodology, the contribution to the SHG coefficient of all the occupied and unoccupied bands are determined by a "band-resolved" scheme<sup>42</sup> and the charge density of the bands is summed up by the SHG-weighted factor and visualized in the real space. Thus, the orbitals dominantly contributed to the SHG coefficient are highlighted whereas those contributed less are not displayed. SHG density analysis is an efficient probe to directly identify the orbitals on which ions or groups contributed to NLO properties, namely hot-spots in real space, and further lead to deep understanding of the origins of the SHG effect in crystals.

## 3. Applications of DFT Method to UV and DUV NLO Crystals

## 3.1. Borate NLO crystals

Due to the good transmission in UV region and the diverse crystal structures, borates are always the research focus in UV NLO crystals field. Till now, except KDP, almost all the applicable UV NLO crystals are borates, e.g., BBO  $(\beta-\text{BaB}_2\text{O}_4)$ , <sup>38</sup> LBO family (LiB<sub>3</sub>O<sub>5</sub>, CsB<sub>3</sub>O<sub>5</sub> and CsLiB<sub>6</sub>O<sub>10</sub>), <sup>43</sup> KBBF family (KBe<sub>2</sub>BO<sub>3</sub>F<sub>2</sub>, RbBe<sub>2</sub>BO<sub>3</sub>F<sub>2</sub> and CsBe<sub>2</sub>BO<sub>3</sub>F<sub>2</sub>), <sup>44</sup> SBBO family (Sr<sub>2</sub>Be<sub>2</sub>B<sub>2</sub>O<sub>7</sub>, K<sub>2</sub>Al<sub>2</sub>B<sub>2</sub>O<sub>7</sub>, BaAl<sub>2</sub>B<sub>2</sub>O<sub>7</sub> and BaAlBO<sub>3</sub>F<sub>2</sub>), <sup>45</sup> YAB (YAl<sub>3</sub>(BO<sub>3</sub>)<sub>4</sub>)<sup>39</sup> and BIBO (BiB<sub>3</sub>O<sub>6</sub>). <sup>46</sup> In these crystals, as shown in Fig. 1 the main structural unit are B–O groups, including the planar anionic (B<sub>3</sub>O<sub>6</sub>)<sup>3–</sup> rings, the continuous network of (B<sub>3</sub>O<sub>7</sub>)<sup>5–</sup> groups and the (BO<sub>3</sub>)<sup>3–</sup> triangles interconnected by (BeO<sub>3</sub>F)<sup>5–</sup>, (AlO<sub>4</sub>)<sup>5–</sup>, (YO<sub>6</sub>)<sup>9–</sup> or (BiO<sub>4</sub>)<sup>5–</sup> polyhedral.

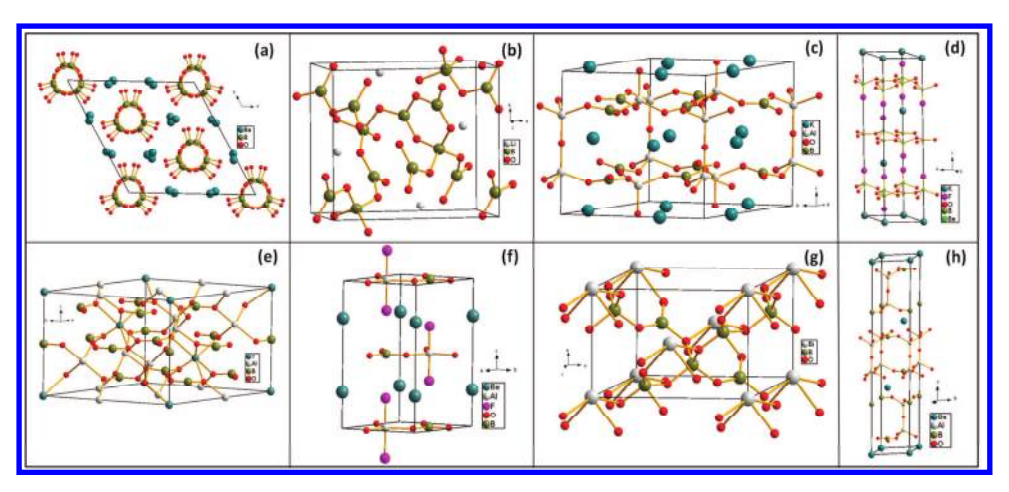


Fig. 1. The crystal structure of the typical borate crystals: (a) BBO, (b) LBO, (c) KABO, (d) KBBF, (e) YAB, (f) BABO, (g) BIBO, (h) BABO.

Table 1. Comparison of experimental and calculated refractive index, birefringence and SHG coefficients (Unit: pm/V) in borate NLO crystals.

			Experin	nental		C	alculated	d
	$n_o$	$n_e$	$\Delta n$	SHG coefficients	$n_o$	$n_e$	$\Delta n$	SHG coefficients
BBO <sup>38</sup>	1.656	1.543	0.113	$d_{22} = \pm 1.60$ $d_{31} \le (0.11 \pm 0.05)$	1.676	1.562	0.114	$d_{22} = -1.32$ $d_{31} = 0.07$
${\rm CLBO^{43}}$	1.485	1.436	0.049	$d_{36} = \pm 0.67$	1.516	1.457	0.059	$d_{36} = 0.546$
${ m KBBF^{41}}$	1.477	1.400	0.077	$d_{11} = 0.49$	1.478	1.413	0.065	$d_{11} = 0.41$
${ m RBBF^{41}}$	1.478	1.407	0.071	$d_{11} = 0.50$	1.4883	1.4295	0.059	$d_{11} = 0.40$
${\rm CBBF^{41}}$	1.501	1.443	0.058	$d_{11} = 0.50$	1.5126	1.4570	0.056	$d_{11} = 0.38$
${\rm KABO^{45}}$	1.559	1.5071	0.052	$d_{11} = 0.45$	1.560	1.492	0.068	$d_{11} = -0.32$
${\rm BABO^{45}}$	1.570	1.517	0.053	$d_{11} = 0.75$	1.5757	1.5257	0.050	$d_{11} = 0.745$
${ m BABF^{47}}$	1.619	1.557	0.042	$d_{22} = 1.10$	1.6664	1.6227	0.044	$d_{22} = 0.70$
$YAB^{39}$	1.759	1.688	0.070	$d_{11} = 1.70$	1.770	1.701	0.069	$d_{11} = 1.657$
BIBO <sup>46</sup>	$n_y =$	1.759 1.785 1.919	0.160	$d_{22} = \pm 2.53$ $d_{16} = \pm 2.8$ $d_{14} = \pm 2.4$ $d_{23} = \mp 1.3$	$n_y =$	1.839 1.779 1.872	0.096	$d_{22} = -2.95$ $d_{16} = -2.55$ $d_{14} = -1.16$ $d_{23} = -1.17$
LBO <sup>43</sup>	$n_y =$	1.566 1.590 1.607	0.041	$d_{31} = \mp 0.98$ $d_{32} = \pm 1.05$ $d_{33} = \pm 0.059$	$n_y =$	1.585 1.599 1.632	0.047	$d_{31} = -0.71$ $d_{32} = 0.84$ $d_{33} = -0.02$
CBO <sup>43</sup>	$n_y =$	1.519 1.550 1.578	0.059	$d_{14} = \pm 0.75$	$n_x =$	1.558 1.581 1.611	0.053	$d_{14} = -0.577$

## 3.1.1. The atom cutting analysis about the borate NLO crystals

The calculated and measured optical properties for the above mentioned borates are listed in Table 1. The good agreement validates the feasibility of plane-wave pseudopotential method to the optical properties of borates. According to the type of A-site cations, these borates can be separated into two categories: A-site cations are alkaline or alkaline earth cations (all mentioned borates except YAB and BIBO), and A-site cations are not alkaline or alkaline earth cations (YAB and BIBO). The real space atom cutting results are listed in Table 2 and some conclusion can be deduced.

Table 2. The calculated and experimental optical properties and the contribution of the respective groups to the optical properties in borates NLO crystals.

BBO	$n_o$	$n_e$	$\Delta n$	$d_{22}$	$d_{31}$	$d_{33}$
$(B_3O_6)^{3-}$	1.5280	1.4114	0.1166	-1.50	-0.039	-0.030
Ba <sup>+</sup>	1.2396	1.2392	0.0004	-0.36	-0.059	0.045
Total	1.6851	1.5695	0.1156	-1.86	-0.098	0.015
Exp.	1.69267	1.66736	0.1247	$\pm 1.60(1 \pm 0.05)$	$\sim 0$	$\sim 0$

Table 2. (Continued)

			Table	2. (Conti	nued)		
LBO	$n_x$	$n_y$	$n_z$	$\Delta n$	$d_{31}$	$d_{32}$	$d_{33}$
$(B_3O_7)^{5-}$	1.564	1.578	1.607	0.043	-0.496	0.571	-0.008
Li <sup>+</sup>	1.048	1.052	1.051	0.004	-0.008	0.002	-0.034
Total	1.557	1.575	1.605	0.045	-0.505	0.582	-0.044
Exp.	1.566	1.591	1.606	0.041	$\pm 0.67$	$\pm 0.85$	$\pm 0.04$
СВО	$n_x$	$n_y$	$n_z$	$\Delta n$		$d_{14}$	
$(B_3O_7)^{5-}$	1.360	1.373	1.414	0.054	_	0.342	
$Cs^{+}$	1.279	1.280	1.285	0.006	_	0.098	
Total	1.557	1.575	1.605	0.048	_	0.577	
Exp.	1.519	1.551	1.578	0.057	±	1.04	
CLBO	n	lo	$n_e$	$\Delta n$		$d_{36}$	
$(B_3O_7)^{5-}$	1.4	19	1.357	0.062	_	0.222	
Li <sup>+</sup>	1.0	290	1.0287	0.0003	_	0.006	
$Cs^+$	1.1	25	1.124	0.001	_	0.138	
Total	1.5		1.455	0.058		0.546	
Exp.	1.4	85	1.436	0.049	±	-0.95	
KBBF	n	l <sub>o</sub>	$n_e$	$\Delta n$		$d_{11}$	
$(BO_3)^{3-}$	1.3	183	1.2242	0.09 4	(	0.376	_
$({\rm BeO_3F})^{5-}$	1.3	088	1.2626	0.046	(	0.113	
$K^{+}$	1.0	874	1.0879	-0.0005	0	0.014	
Total	1.4	694	1.4069	0.063	C	0.41	
Exp.	1.4	77	1.400	0.077	(	).49	
RBBF	n	lo	$n_e$	$\Delta n$		$d_{11}$	
$(BO_3)^{3-}$	1.3	551	1.2766	0.079	(	0.369	_
$({\rm BeO_3F})^{5-}$	1.3	458	1.3113	0.035	0	0.126	
$Rb^+$	1.1	884	1.1928	-0.0044	0	0.030	
Total	1.4	883	1.4295	0.059	0	0.40	
Exp.	1.4	78	1.407	0.071	C	0.50	
CBBF	n	l <sub>o</sub>	$n_e$	$\Delta n$		$d_{11}$	
$(BO_3)^{3-}$	1.4	221	1.3607	0.061	(	0.359	
$({\rm BeO_3F})^{5-}$	1.3	690	1.3371	0.032	C	0.124	
$\mathrm{Cs}^+$	1.4	532	1.4270	0.026	0	0.128	
Total		126	1.4570	0.056		0.38	
a[1pt] Exp.	1.5	01	1.443	0.058	(	0.50	
BABO	n	lo.	$n_e$	$\Delta n$		$d_{11}$	
$(BO_3)^{3-}$	1.3	423	1.2711	0.071		0.348	
$(AlO_4)^{5-}$	1.3	876	1.3818	0.006	(	0.267	
$\mathrm{Ba^{2+}}$	1.1	616	1.1492	0.012	C	0.115	
Total	1.5	757	1.5257	0.050		).75	
Exp.	1.6	98	1.636	0.062	(	).745	

			Table 2.	(Contin	rueu)			
KABO	n	l <sub>o</sub>	$n_e$	$\Delta n$		$d_1$	1	
$(BO_3)^{3-}$	1.3	311	1.256	0.055		0.1	52	
$(AlO_4)^{5-}$	1.5	367	1.349	0.018		0.2	83	
$K^{+}$	1.1	125	1.124	0.001		-0.0	012	
Total	1.5	527	1.478	0.049		0.4	15	
Exp.	1.5	560	1.492	0.068		0.3	17	
BABF	n	l <sub>o</sub>	$n_e$	$\Delta n$		$d_2$	2	
$(BO_3)^{3-}$	1.4	490	1.3799	0.0691		0.3	23	
$(AlF_2O_3)^{5-}$	1.5	081	1.4899	0.0182		0.2	33	
$\mathrm{Ba}^{2+}$	1.2	612	1.2507	0.0105		0.0	92	
Total	1.7	698	1.7152	0.0546		0.7	02	
Exp.	1.6	619	1.557	0.042		1.1	.0	
BIBO	$n_x$	$n_y$	$n_z$	$\Delta n$	$d_{22}$	$d_{16}$	$d_{14}$	$d_{23}$
$(BO_3)^{3-}$	1.5514	1.5242	1.5991	0.0749	-0.233	-0.628	0.372	0.243
$(BO_4)^{5-}$	1.4014	1.3782	1.4240	0.0458	-0.118	-0.334	0.391	0.050
$(BiO_4)^{5-}$	1.6922	1.6388	1.6746	0.0534	-2.829	-2.090	-1.412	-1.182
Original	1.8391	1.7792	1.8717	0.0925	-2.95	-2.55	-1.16	-1.17
Exp.	1.7585	1.7854	1.9190	0.1605	$\pm 2.53$	$\pm 2.8$	$\pm 2.4$	∓1.3
YAB	n	le	$n_o$	$\Delta n$		$d_1$	1	
Al <sup>3+</sup>	1.0	483	1.0525	0.0042		-0.0	001	
$(BO_3)^{3-}$	1.0	666	1.4362	0.0696		0.6	85	
(DO3)	1.3	000						
$(YO_6)^{9+}$		290	1.4385	0.0095		1.4	21	
	1.4					1.4 1.6		

## (1) For the crystals whose A-site cations are alkaline or alkaline earth cations:

Although the A-site cations make some contribution to the refractive index, they almost contribute nothing to the birefringence. This resulted from the fact that their electron clouds are nearly spherical and the responses to the incident light are almost isotropic. (i) The A-site cations contribute increasingly to the SHG response and birefringence with the increasing radii. For instance, in KBBF family crystals, K<sup>+</sup> contributes to no more than 1% and 5% to birefringence and  $d_{11}$  in KBBF, while in CBBF, the contribution of Cs<sup>+</sup> to birefringence and  $d_{11}$  are both around 20%. However, it should be emphasized in all crystals the alkaline or alkaline earth cations contribute no more than 20% to the birefringence and SHG response. (ii) The SHG response is mainly originated from contribution of B–O groups i.e.,  $(B_3O_6)^{3-}$  groups in BBO,  $(B_3O_7)^{5-}$  groups in LBO family crystals and  $(BO_3)^{3-}$  groups in KBBF and SBBO family crystals. It is because the B–O groups with three-coordinated boron ions have strong anisotropic response to the incident light. The real space atom cutting analysis results actually con-

firm the conclusion from the anionic groups theory proposed by Chen, <sup>19</sup> which states that the macroscopic SHG coefficients are mainly determined by the microscopic second-order polarizability of the anionic groups in UV and DUV NLO crystals.

(2) For the crystals whose A-site cations are not alkaline or alkaline earth cations:

For the borates listed in Table 1, in BIBO and YAB the A-site cations are Bi<sup>3+</sup> and Y<sup>3+</sup>, respectively. The first-principles electron structure calculation reveals that the distribution of charge density around Bi or Y is distorted from the spherical shape seriously, due to the strong covalent bond formed with the neighbor oxygen atoms. Consequently, in the atom cutting analysis, not isolated Bi<sup>3+</sup> and Y<sup>3+</sup> ions but the  $(BiO_4)^{5-}$  quadrangular pyramids and deformed  $(YO_6)^{9-}$  octahedra were treated as the whole atom-cutting unit. The atom-cutting results on the two crystals revealed that (i) in BIBO, the coplanar (BO<sub>3</sub>)<sup>3-</sup> groups contribute mostly to the birefringence, but the SHG response mainly originate from the  $(BiO_4)^{5-}$  quadrangular and the contribution of (BiO<sub>4</sub>)<sup>5-</sup> quadrangular to the SHG coefficient exceed 90%. The large SHG response of  $(BiO_4)^{5-}$  mainly result from the fact that  $(BiO_4)^{5-}$ groups is deformed tetragonals and the stereochemical long pair electrons exists in the bismuth cations. (ii) In YAB, the Al<sup>3+</sup> cations almost contribute nothing to the birefringence and SHG coefficient. The birefringence mainly is mainly determined by the coplanar (BO<sub>3</sub>)<sup>3</sup> groups, while the SHG coefficient mainly comes from the  $(YO_6)^{9-}$  distorted tetrahedra. The large second-order susceptibility of  $(YO_6)^{9-}$ originated from the second order John-Teller effect resulted from the strong octahedral distortion, similar to the  $(NbO_6)^{7-}$  and  $(TiO_6)^{8-}$  groups in LiNbO<sub>3</sub> (Ref. 48) and BaTiO<sub>3</sub>,<sup>49</sup> respectively.

### 3.1.2. The SHG density analysis in borates

To intuitively identify the hot-spot of the SHG effect, BBO and YAB crystals are selected to demonstrate the SHG density analysis<sup>39</sup>.

Figure 2 displays the charge density and SHG density around the  $\mathrm{Ba^{2+}}$  cations and  $(\mathrm{B_3O_6})^{3-}$  groups in BBO. It is clearly shown that although considerable charge density exists around  $\mathrm{Ba^{2+}}$  cations, they almost contribute nothing to the SHG coefficient. The charge contributing to the SHG efficient mainly assemble at the O 2p orbitals in the  $(\mathrm{B_3O_6})^{3-}$  groups. This result is consistent with the conclusion deduced by the atom-cutting analysis. Figure 3 plotted the SHG density maps on the  $(\mathrm{BO_3})^{3-}$  and Y–Al planes in YAB. Clearly, the SHG effect mainly comes from the contribution of the orbitals on the  $(\mathrm{BO_3})^{3-}$  groups and  $(\mathrm{YO_6})^{9-}$  groups and the contribution of  $\mathrm{Al^{3+}}$  cations is neglectably small. This result verified the result obtained by atom cutting method, i.e., the SHG effect of YAB mainly originates from the  $(\mathrm{BO_3})^{3-}$  and  $(\mathrm{YO_6})^{9-}$  groups and the contribution of  $(\mathrm{YO_6})^{9-}$  octahedral is much larger than that of  $(\mathrm{BO_3})^{3-}$  triangles.

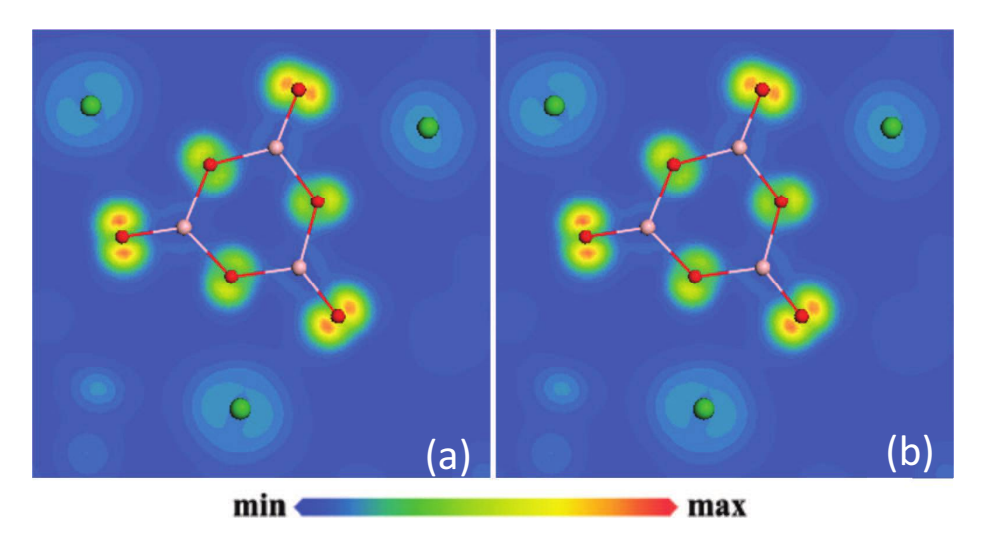


Fig. 2. (a) Charge density (b) SHG density around  $(B_3O_6)^{3-}$  group in BBO, Ba, B and O atoms are represented by green, pink and red balls, respectively.

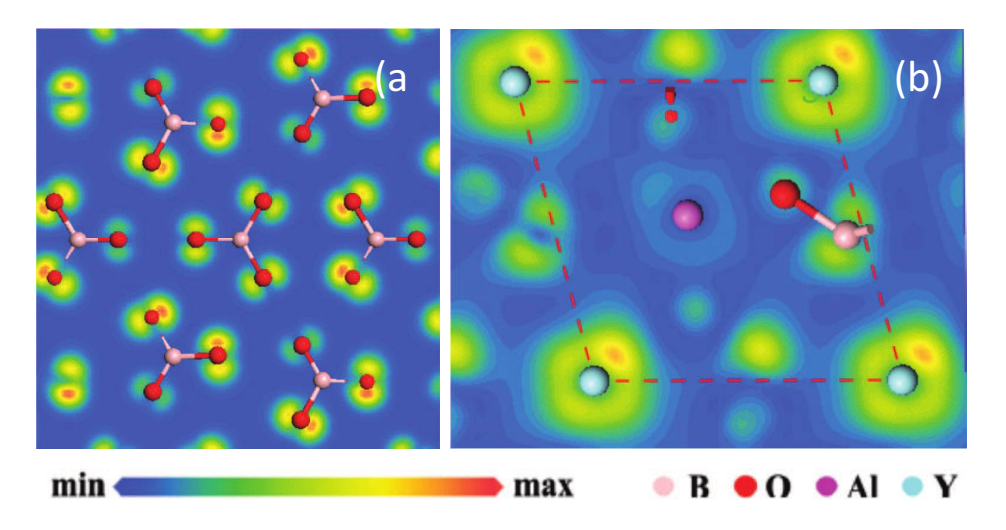


Fig. 3. The SHG densities on around (BO<sub>3</sub>) groups (a) and in Y-Al planes (b) in YAB.

# 3.2. $KH_2PO_4$ (KDP)

KDP is the first commercially used SHG and optic-electric crystal. Owing to its excellent optical properties and mature growing technology, KDP is still widely used in SHG device and popular as optic-electric materials. $^{50-53}$  At room temperature, KDP belongs to acentric I $^{4}$ 2d space groups, in which the fundamental PO<sub>4</sub> tetrahedral are bonded by the hydroxy bonds between the H atoms and O atoms in the

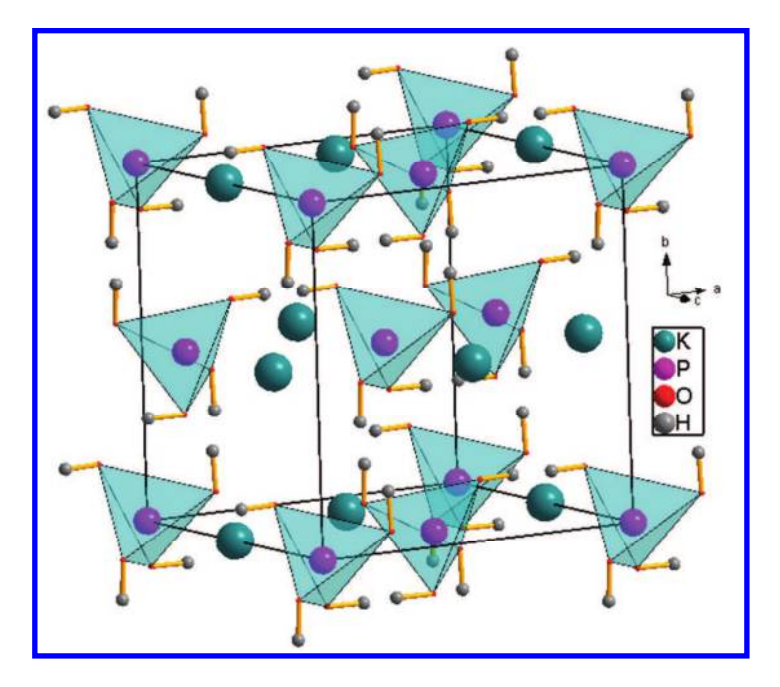


Fig. 4. The unit cell of KDP.

Table 3. The calculated and experimental optical properties and the atom-cutting analysis of KDP.

	$n_o$	$n_e$	$\Delta n$	$d_{36}$
Exp.	1.49535	1.46041	0.035	0.39
Cal.	1.5518	1.5104	0.0415	0.42
K	1.1125	1.1112	0.0013	0.004
$PO_4$	1.4649	1.4402	0.0247	0.417
$H_2PO_4$	1.4977	1.4482	0.0495	0.421

hydroxy groups of the O's of PO<sub>4</sub> and the K<sup>+</sup> cations are embedded in the cavity of the framework formed by the PO<sub>4</sub> (shown in Fig. 4).

For decades, much theoretical effort have been devoted to go insight to the mechanism of the related properties of KDP. However, the *ab initio* studies were mainly focused on the electron structure and ferroelectric transition.  $^{54,55}$  So it is of great significance to explore the nonlinear optical properties by first principles calculation. Table 3 lists the calculated and experimental linear and NLO properties,  $^{56}$  which shows a very good agreement with the measured values. Moreover, The atom-cutting results (also listed in Table 3) demonstrate that the K<sup>+</sup> cation contributes almost nothing to both the birefringence and SHG coefficient due to its strong ionic characteristic, although it has a little contribution to the optical refractive indices. The comparison of the  $(PO_4)^{3-}$  groups and  $(H_2PO_4)^{1-}$  groups reveals that the hydrogen bond determines the linear optical anisotropy (i.e., the

birefringence  $\Delta n$ ) in KDP, but its contribution to the SHG effect is neglectably small. The SHG effect in KDP mainly originated from the  $(PO_4)^{3-}$  groups.

# 3.3. Evaluation and molecular engineering design of the UV NLO carbonate crystals

## 3.3.1. The evaluation of UV NLO carbonate crystals

For decades, the exploration of deep-UV (DUV, wavelength less than 200 nm) NLO crystals has always focused on the borates. In fact, analogue to  $(BO_3)^{3-}$  groups, coplanar  $(CO_3)^{3-}$  groups are also expected to be the good NLO microstructure unit since this planar triangle structure with  $\pi$ -conjugated molecular orbitals can produce the large second-order susceptibility and birefringence. In particular, the fluoride carbonates with the formula  $A_l(CO_3)_k F_m$  (A = alkaline and/or alkalineearth metal elements)<sup>11</sup> invoke our specific interests because the introduced fluorine atoms and connection of between the atoms with relative strong electronegativity and terminal oxygen atoms of CO<sub>3</sub> groups are beneficial to the generation of large band gap. Recently, several carbonate crystals have been discovered, 11,57,58 showing good potential as DUV NLO crystals. However, in the initial stage of these material synthesis, only the small single crystals or powders have been obtained and it is difficult to perform the comprehensive assessment in experiment to evaluate their applying prospect in the DUV NLO field. In this case, the first-principles provide a rapid and effective way to investigate the prospect of these crystals in UV and DUV application.

After exploring all the carbonates in the inorganic crystal structure database (ICSD), seven noncentrosymmetric carbonates with the formula  $A_l(CO_3)_k F_m$ were found, i.e., KCaCO<sub>3</sub>F, KSrCO<sub>3</sub>F, RbCaCO<sub>3</sub>F, RbSrCO<sub>3</sub>F, CsCaCO<sub>3</sub>F,  $Cs_3Ba_4(CO_3)_3F_5^{11}$  and  $NaCa_3(CO_3)_3F_3 \cdot H_2O^{60}$ . The last one is not suitable for the DUV NLO application due to its hydration. The other six crystals were catalogued to three classes according to their structural features, as shown in Fig. 5(a) the coplanar  $(CO_3)^{2-}$  triangles are flat-lying with the exact parallel orientation; 5(b) the coplanar (CO<sub>3</sub>)<sup>2-</sup>triangles are flat-lying with the partly antiparallel orientation; and 5(c) (CO<sub>3</sub>)<sup>2-</sup> groups are standing-on-edge with respect to the overall structural layering. The first-principles calculated and available experimental optical properties are listed in Table 4, and their good agreement confirms the feasibility of plane-wave pseudopotential method in the fluoride carbonates. More importantly, according to the detailed comparison of the optical properties among the three types of carbonates, we can see that the fluorine carbonates with the  $(CO_3)^{2-}$  groups in flat-lying structure always possess larger birefringence (> 0.1) and they are suitable to be the birefringent crystals which can be used for polarizers, beam displacers and beam splitters in the UV region. In contrast, the fluorine carbonates (Cs<sub>3</sub>Ba<sub>4</sub>(CO<sub>3</sub>)<sub>3</sub>F<sub>5</sub>) with (CO<sub>3</sub>)<sup>2-</sup> groups in standing-on-edge arrangement has much smaller birefringence and is not suitable for the UV harmonic generation. All the fluorine carbonates with the  $(CO_3)^{2-}$  groups in flat-lying structure have the

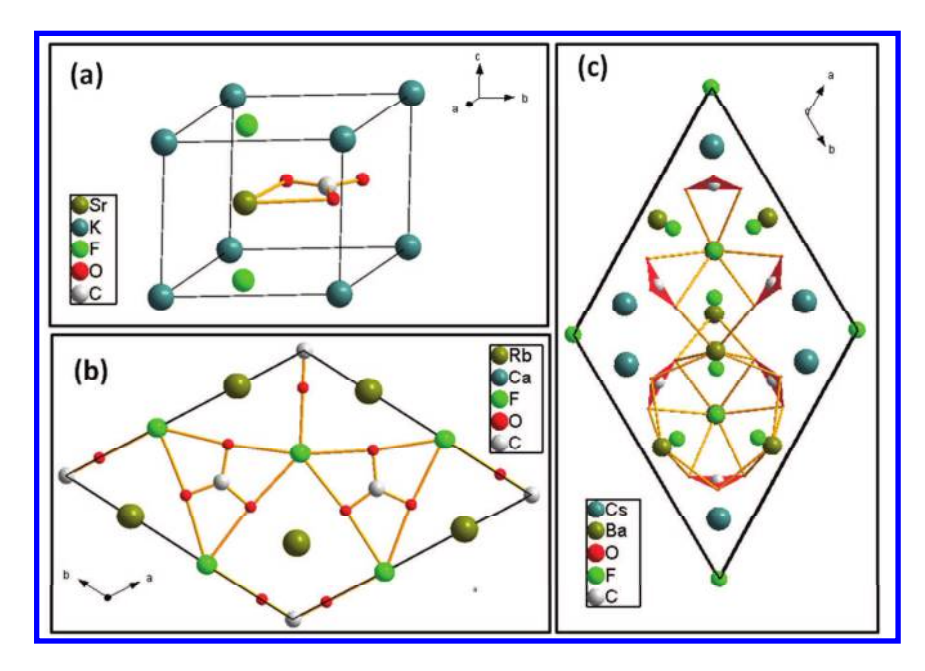


Fig. 5. The three types crystal structures of the UV fluoride carbonates: (a) the (CO<sub>3</sub>) groups are flat-lying with the orientation exactly parallel, (b) the (CO<sub>3</sub>) groups are flat-lying but partly antiparallel, (c) the (CO<sub>3</sub>) groups (represented by red triangles) are standing-on-edge with respect to the overall structural layering.

Table 4. The calculated and experimental linear and nonlinear optical properties of fluorine carbonate. The KBBF and BABF are also listed for comparison.

	Exp.PSHG (pm/V)	Cal.PSHG (pm/V)	Cal.SHG coeff. (pm/V)	$n_o$	$n_e$	$\Delta n$	λ PM (nm)
KSrCO <sub>3</sub> F	1.30	0.96	$d_{11} = 1.38$	1.5316	1.4269	0.105	198
$RbSrCO_3F$	1.30	0.98	$d_{11} = -1.43$	1.5630	1.4610	0.102	195
$KCaCO_3F$	1.41	0.82	$d_{11} = -1.19$	1.5303	1.4188	0.112	197
$RbCaCO_3F$	0.43	0.24	$d_{22} = -0.35$	1.5515	1.4360	0.116	198
$CsCaCO_3F$	0.43	0.31	$d_{22} = 0.45$	1.5939	1.4870	0.107	195
$\mathrm{Cs_3Ba_4}(\mathrm{CO3})_3\mathrm{F}_5$	0.47	0.57	$d_{31} = 0.554, d_{33} = -0.75$	1.5742	1.6079	0.034	315
BABF	$d_{22} = 1.24$	0.53	$d_{22} = 1.10$	1.619	1.557	0.042	273
KBBF	$d_{11} = 0.49$	0.21	$d_{11} = 0.49$	1.477	1.400	0.077	161

stronger SHG effect than that in borates. Therefore, these carbonates are all very good NLO candidate crystals for the generation of 266 nm coherent laser which is in very great industrial demand.

#### 3.3.2. The molecular engineering design of the UV NLO carbonate crystals

It should be mentioned that all existing fluorine carbonates have the UV absorption edge larger than 195 nm (i.e., the energy band gap less than 6.3 eV). This means

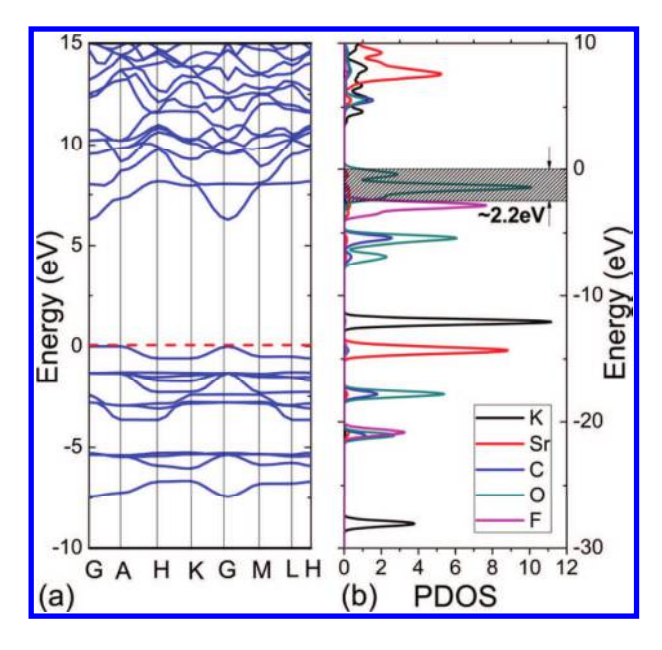


Fig. 6. (a) The electron band structure and (b) the partial density of state projected to the constitute atoms of KSrCO<sub>3</sub>F. The shadow part in the PDOS indicates the non-bonding O 2s orbitals.

that all of them cannot be used in the harmonic generation of the coherent light in DUV region. Driven by the idea to explore the NLO crystals having the larger band gap in fluorine carbonate, we studied the electron structures of the crystals in Sec. 3.3.1. According to the PDOS plotted in Fig. 6, one can see that the O-2s orbitals are located at the top of VB and hybridized little with other orbitals, so forming the non-bonding states (or dangling bonds) and determining the band gaps in the fluorine carbonates. We considered that these nonbonding states can be eliminated by the incorporating the cations with strong electronegativity and the band gaps would be very likely to reach the DUV region.

With the guidance of this idea, we systematically substituted the  $Ca^{2+}$ ,  $Sr^{2+}$  or  $Ba^{2+}$  cations with  $Be^{2+}$  and  $Al^{3+}$  which have stronger electronegativity in the  $A_l(CO_3)_kF_m$  family, and theoretically obtained two novel fluoride carbonates,  $^{61}$  KBeCO<sub>3</sub>F and RbAlCO<sub>3</sub>F<sub>2</sub>. Both crystals are kinetically stable (i.e., no imaginary frequency were detected in the phonon spectra), and their atomic structure are displayed in Fig. 7. The first-principles calculations reveal that both KBeCO<sub>3</sub>F and RbAlCO<sub>3</sub>F<sub>2</sub> possess good transmission in DUV region with the energy band gaps of 7.61 eV and 8.21 eV, respectively. Moreover, their birefringence (0.13 and 0.10 for KBeCO<sub>3</sub>F and RbAlCO<sub>3</sub>F<sub>2</sub>) and SHG effect ( $d_{21} = -0.94$  pm/V for KBeCO<sub>3</sub>F and  $d_{16} = -0.69$  pm/V for RbAlCO<sub>3</sub>F<sub>2</sub>) are enough to effectively generate the SHG wave in the DUV region. Once synthesized in experiments, KBeCO<sub>3</sub>F and RbAlCO<sub>3</sub>F<sub>2</sub> would have wide NLO applications in the DUV region.

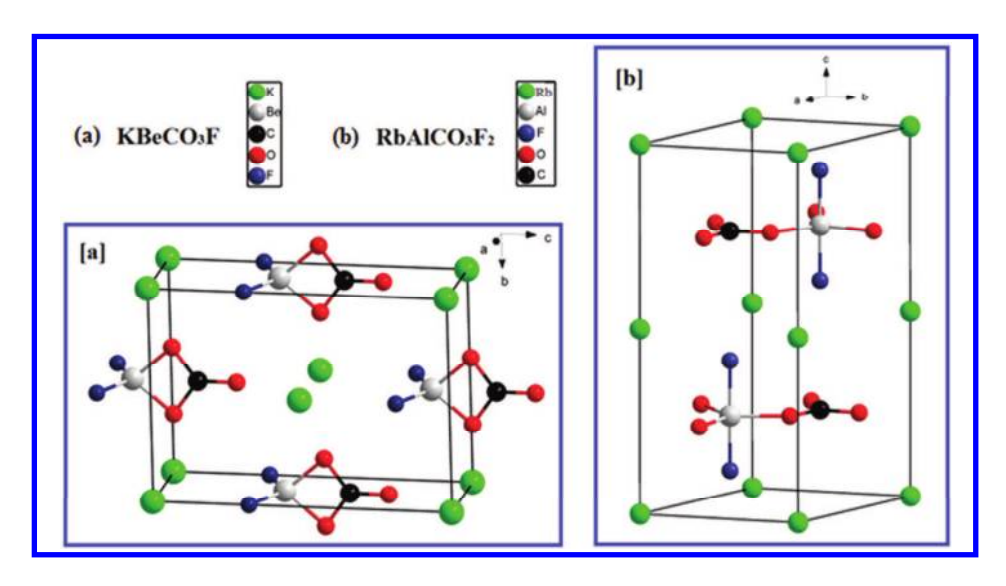


Fig. 7. The crystal structure of (a) KBeCO<sub>3</sub>F and (b) RbAlCO<sub>3</sub>F<sub>2</sub>.

## 4. The Applications of DFT Method to IR NLO Crystals

## 4.1. Metal chalcogenides

Up to now, most of IR NLO crystals belong to the chalcopyrite structure, in which  $\text{LiGaX}_2$  and  $\text{AgGaX}_2$  (X = S, Se, Te)<sup>62,63</sup> crystals are the widely used IR NLO crystals due to the large SHG effect, good transmission in IR region and mature single-crystal growth method. As depicted in Fig. 8, all the crystals share the sim-

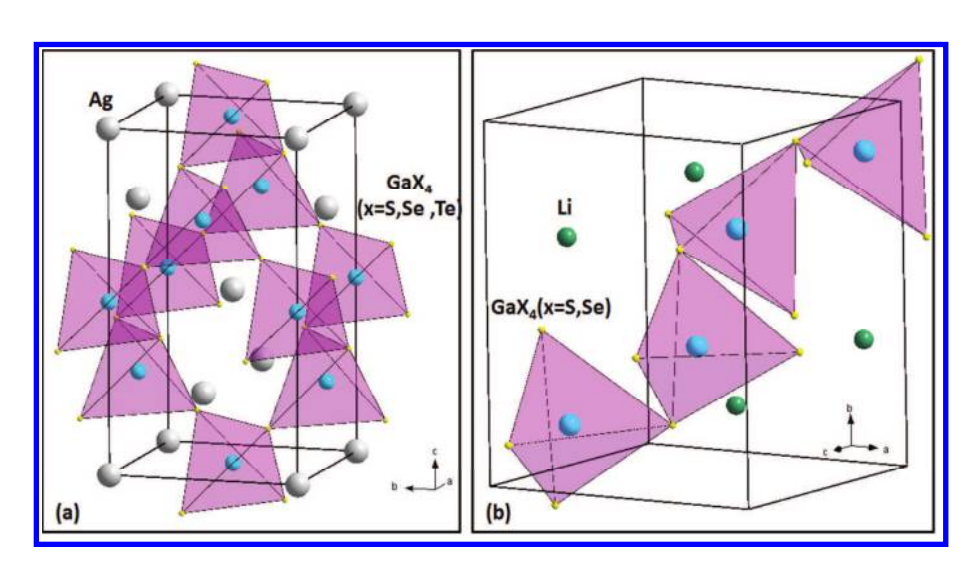


Fig. 8. The crystal structure of (a)  $AgGaX_2$ , (b)  $LiGaX_2$  (X = S, Se and Te).

ilar structural feature: the gallium atoms are four-coordinated with X atoms and the cations are embedded in the cavity formed by the  $GaX_4$  tetrahedra. It is interesting that the larger energy band gaps and smaller SHG effects are possessed in  $LiGaX_2$  compared with their counterpart in the  $AgGaX_2$  family. Meanwhile, the birefringence in the former is larger than that in the latter crystals.

The calculated and experimental optical properties as well as the atom cutting analysis are listed in Table 5. One can see that the calculated linear and NLO crystals are in good accordance with the experimental values, confirming the feasibility of the DFT method to both the two family crystals.<sup>62,63</sup> According to the result of atom cutting analysis, in both families the birefringence and SHG coefficient mainly originated from the GaX<sub>4</sub> tetrahedral. This is because the Ga-X bonds possess much more covalent characteristic and exhibit much more optical anisotropy compared with the Li-X or Ag-X bonds. Moreover, the larger birefringence in LiGaX<sub>2</sub> than that of AgGaX<sub>2</sub> resulted from the fact that the GaX<sub>4</sub> tetrahedral are more deformed in the former than in the latter. However, the contribution of Ag+ cations to the refractive indices and SHG coefficients are much more prominent than that of Li<sup>+</sup>. The detailed PDOS analysis reveals that in LiGaX<sub>2</sub> the orbitals on Li<sup>+</sup> cations almost contribute nothing to the electronic states in the top of VB. As comparison, a few Ag d-orbitals are located at both the top of VB and the bottom of CB, narrowing the energy band gaps in AgGaX<sub>2</sub>. Since energy band gap is inversely proportional to the SHG coefficient in the fifth power approximately [see formula (2)], AgGaX<sub>2</sub> have the larger SHG effects than those in  $LiGaX_2$ .

Apart from the LiGaX<sub>2</sub> and AgGaX<sub>2</sub> crystals, the DFT method also has been successfully used to investigate the NLO mechanism and evaluate the application prospect of many newly discovered metal chalcogenides, such as BaGa<sub>4</sub>Se<sub>7</sub>,  $^{64}$  BaAl<sub>4</sub>Se<sub>7</sub>,  $^{65}$  Ba<sub>6</sub>Sn<sub>6</sub>Se<sub>13</sub>,  $^{66}$  NaBa<sub>4</sub>Ge<sub>3</sub>S<sub>10</sub>Cl,  $^{67}$  etc. These studies demonstrate the importance of DFT simulation method on the NLO crystal explorations in this materials field.

## 4.2. The structural selection of mid-IR halide NLO crystals

Up to now, the existing commercially used IR NLO crystals usually possess large SHG coefficient, such as  $AgGaX_2$  (X = S, Se, Te), <sup>68</sup>  $ZnGeP_2^{69}$  and  $LiBX_2^{70}$  (B = Al, Ga, In and X = S, Se, Te). However, according to the formula (2), the larger SHG coefficients are usually accompanied by the small band gaps. It is well known that the laser damaging threshold (LDT) is closely positively related to the band gaps and small band gaps usually cause low LDT. Consequently, the key issue to exploring the NLO crystals in mid-IR region is to find the balance between the band gaps and SHG response. The relation between LDT and energy band gap plotted in Fig. 9 clearly shows that a mid-IR NLO crystal should have the energy band gap larger than 3.0 eV at best, if the LDT of the crystals needs to be larger than  $100 \text{ W/cm}^2$  for a nanosecond laser. At the same time, to guarantee the high output

Table 5. The calculated and measured linear and nonlinear optical properties and the atom cutting analysis of LiGaX<sub>2</sub> (Ref. 66 and AgGaX<sub>2</sub> (Ref. 65) (X = S, Se and Te) crystals.

LiGaS <sub>2</sub>	$n_x$	$n_y$	$n_z$	$\nabla u$	$d_{31} \text{ (pm/V)}$	$d_{31} \text{ (pm/V)}  d_{32} \text{ (pm/V)}  d_{33} \text{ (pm/V)}$	$d_{33} \text{ (pm/V)}$	$AgGaS_2$	$n_o$	$n_e$	$\nabla u$	$d_{36} \text{ (pm/V)}$
Li+	1.1234	1.1226	1.1181	0.0053	0	0	0	$Ag^+$	1.4373	1.4341	0.0032	0.52
$GaS_2^-$	2.1798	2.125	2.1224	0.0574	-3.80	-3.10	7.01	$GaS_2^-$	2.3503	2.3364	0.0139	14.84
Original	2.1972	2.1403	2.14	0.0572	-3.80	-3.10	7.2	Original	2.584	2.553	0.031	14.1
Experimental	2.0674	2.1048	2.1073	0.0572	-5.8	-5.12	10.7	Experimental	2.4486	2.3954	0.0532	11.0, 12.5
$LiGaSe_2$	$n_x$	$n_y$	$n_z$	$\nabla n$	$d_{31} \text{ (pm/V)}$	$d_{32} \text{ (pm/V)}$	$d_{33} \text{ (pm/V)}$	AgGaSe 2	$n_o$	$n_e$	$\nabla n$	$d_{36} \text{ (pm/V)}$
Li+	1.1274	1.1268	1.1258	0.0015	0	0	0	$^{+}\mathrm{Ag}^{+}$	1.4676	1.463	0.004	1.18
$GaSe_2^-$	2.319	2.3112	2.3257	-0.0145	-6.25	-4.55	13.05	$GaSe_2^-$	2.7355	2.7275	0.008	46.25
Original	2.3356	2.3258	2.3423	0.0165	-6.25	-4.60	13.45	Original	2.9798	2.9358	0.044	45.2
Experimental	2.2373	2.2849	2.2882	0.0509	10	7.7	-18.2	Experimental	2.8932	2.8452	0.048	33
$LiGaTe_2$	$n_o$	$n_e$	$\nabla n$			$d_{36} \; (\mathrm{pm/V})$		${ m AgGaTe}_2$	$n_o$	$n_e$	$\Delta n$	$d_{36} \text{ (pm/V)}$
Li+	1.4611	1.4504	0.0107			-0.70		$^{+}\mathrm{Ag}^{+}$	1.4442	1.4497	-0.0055	2.22
${ m GaTe}_2^-$	2.7901	2.8264	-0.0363			-49.55		${ m GaTe}_2^-$	3.009	3.0541	-0.0451	06
Original	2.8101	2.8421	0.032			-50.4		Original	3.2678	3.2799	-0.0115	99.5
Experimental						-42		Experimental	2.9859	3.0047	-0.0188	

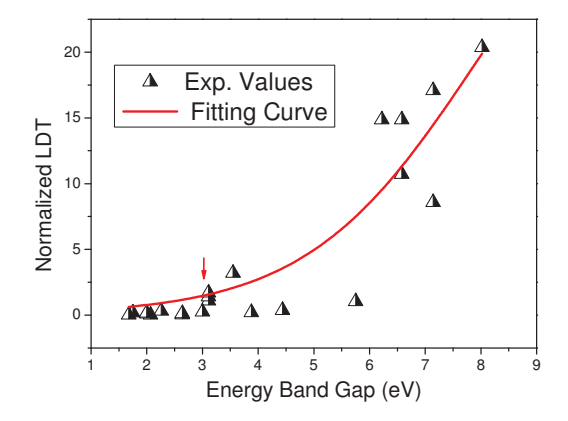


Fig. 9. The dependence of the laser damage threshold on the band gaps for the NLO crystals. The LDT is normalized to about  $100~\mathrm{MW/cm^2}$  for a nanosecond laser (indicated by a red arrow) which is enough for almost all academic and commercial purposes.

power, the SHG effect in crystal should be larger than  $\sim 10 \times \text{KDP}$ . These technical parameters are good enough for almost all the current academic and commercial applications for mid-IR NLO crystals.

Recently, several halide-based mid-IR NLO crystal are reported. These crystals possess good transmission in mid-IR region, relatively large SHG coefficient, moderate birefringence and high LDT. Furthermore, the structures of many halide-based

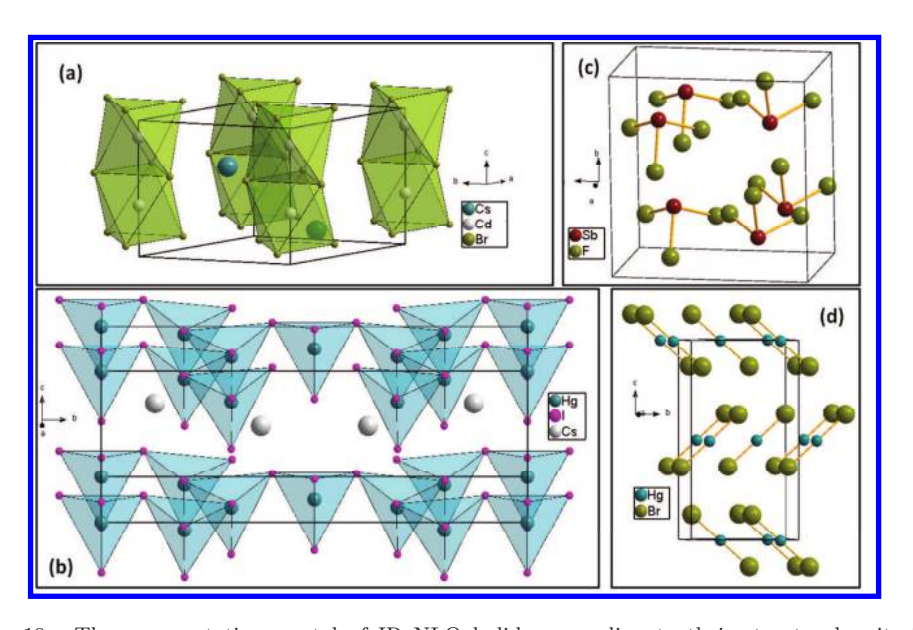


Fig. 10. The representative crystal of IR NLO halides according to their structural units in (a)  $CsCdBr_3$  for  $[MX_6]$  distorted octahedra, (b)  $CsHg_3Br_9$  for  $[MX_4]$  tetrahedra, (c)  $SbF_3$  for  $MX_3$  triangular-pyramids (d)  $HgBr_2$  for  $[MX_2]$  one-dimensional strings.

materials are consistent with the criterion of the mid-IR NLO crystal with good performance. Therefore, the systematical studies on the optical properties and mechanisms in halide crystals, either experimentally or theoretically, are still lacking. Besides, many halides were just obtained in the form of powder or small single crystals which are impractical to perform the comprehensive experimental measurement. Therefore, the first-principles calculations can provide a rapid and efficient way to perform the performance assessment and give the insight to the structure-properties relation in these materials at atomic level. Based on the structural features, the mid-IR halide-based crystals can be catalogued to four types according to the anionic groups  $[MX_k]$  (M = center cation, X = halide anion, k = 6, 4, 3 and 2, representing distorted octahedral, tetrahedral, triangular-pyramids and one-dimensional strings, respectively), and the corresponding basic structures are displayed in Fig. 10.

The optical properties, including the energy band gaps, refractive indices, bire-fringence and SHG coefficients for the chosen mid-IR halide crystals were calculated, and the results are listed in Table 6. It is revealed that  $[MX_4]$ ,  $[MX_3]$  or  $[MX_2]$  units in these materials are suitable to generate relatively large birefringence (usually larger than 0.06), while the nearly optical isotropic  $[MX_6]$  octahedra produce much smaller birefringence ( $\Delta n$  typically less than 0.01) that cannot satisfy the requirement for NLO output in the mid-IR region. The fluorides possess large energy band gap but small SHG effect, while the iodides possess large SHG effect

Table 6. The calculated and experimental linear and NLO properties of the halides NLO crystals.

		$n_x$	$n_y$	$n_z$	n	SHG coefficients (pm/V)	PSHG effect (pm/V)
	$CsGeF_3^*$	1.6332	1.6331	1.6330	0.000	$d_{15} = -0.20, d_{22} = 0.34, d_{33} = 0.34$	1.09
	$CsGeCl_3$	1.9053	1.9052	1.9051	0.000	$d_{15} = 1.10, d_{22} = -0.79, d_{33} = -0.77$	$3.91(\sim 5)$
$[MX_6]$	$CsGeBr_3$	2.1585	2.1582	2.1579	0.001	$d_{15} = 4.50, d_{22} = 0.35, d_{33} = 0.43$	$14.39(\sim 10)$
	$CsGeI_3$	2.2702	2.2693	2.2684	0.002	$d_{15} = 3.58, d_{22} = 19.03, d_{33} = 19.28$	40.30
	$CsCdBr_3$	1.8920	1.8926	1.8998	0.008	$d_{15}=0.06,d_{24}=0.06,d_{33}=0.10$	$0.24(\sim 2)$
	$\text{Cs}_2\text{Hg}_3\text{Cl}_8*$	1.9982	1.9689	2.0291	0.061	$d_{11} = 6.97, d_{15} = 3.00, d_{12} = -3.84,$ $d_{13} = -5.01, d_{24} = 6.94, d_{33} = -7.97$	22.4
$[MX_4]$	$\text{Cs}_2\text{Hg}_3\text{Br}_8*$	2.1767	2.0769	2.1753	0.099	$d_{11} = 16.98, \ d_{15} = 5.08, \ d_{12} = -7.62, \\ d_{13} = -9.02, \ d_{24} = 12.10, \ d_{33} = -13.27$	41.6
	$\text{Cs}_2\text{Hg}_3\text{I}_8$	2.2395	2.1473	2.2417	0.094	$d_{11} = 27.59, \ d_{15} = 4.15, \ d_{12} = -14.12, \\ d_{13} = -15.66, \ d_{24} = 21.10, \ d_{33} = -18.73$	$68.5(\sim 32)$
	$NaSb_3F_{10}$	1.7218	1.7218	1.6217	0.100	$d_{15} = -0.31, d_{33} = -0.83$	1.64(3.2)
	${\rm NaSb_3Cl_{10}}^*$	2.1416	2.1416	1.9715	0.170	$d_{15} = -0.92, d_{33} = 1.28$	2.91
	${\rm NaSb_3Br_{10}}*$	2.3512	2.3512	2.1162	0.235	$d_{15} = 0.03, d_{33} = 7.87$	10.18
	$NaSb_3I_{10}*$	2.7685	2.7685	2.4016	0.367	$d_{15} = 4.72, d_{33} = 29.04$	44.00
$[MX_3]$							
	$SbF_3$	1.7634	1.6979	1.8425	0.145	$d_{11} = 1.63, d_{12} = 0.27, d_{13} = 0.17$	2.39(5.8)
	SbCl <sub>3</sub> *	2.1339	2.0196	2.2314	0.212	$d_{11}=5.12,d_{12}=3.45,d_{13}=-7.29$	14.64
	${ m SbBr_3}^*$	2.3576	2.2065	2.5018	0.295	$d_{11} = 5.81, d_{12} = 6.36, d_{13} = -10.36$	21.18
	SbI <sub>3</sub> *	2.9971	2.5213	3.4453	0.924	$d_{11} = 22.06, d_{12} = 15.58, d_{13} = -63.24$	117.03
$[MX_2]$	HgBr <sub>2</sub>				0.238		$\sim 10 \times \text{KDP}$

<sup>\*</sup>Hypothetical crystals.

The value in the parentheses are the measured result.

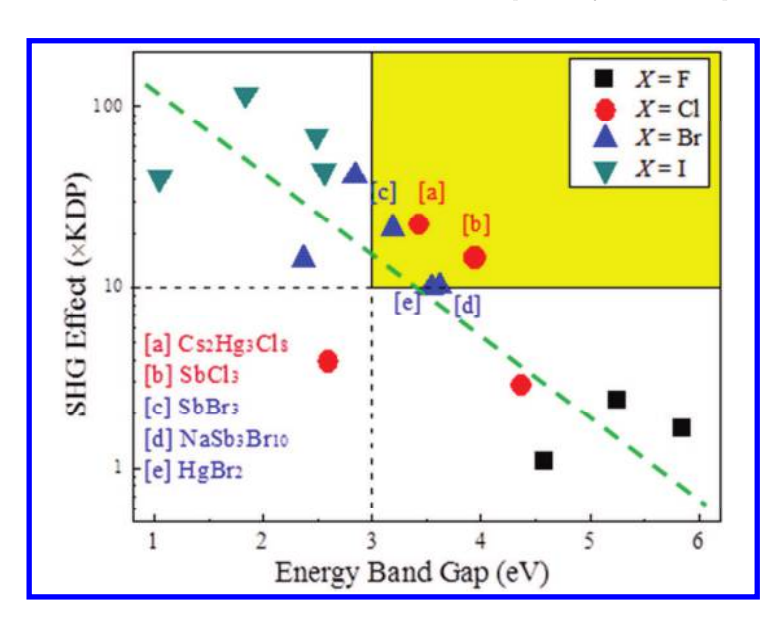


Fig. 11. The distribution of the SHG effect on the band gaps for all the halide studied. It is clear that a negative correlation exists between the band gaps and SHG effect as indicated by the dash line fitted by least square method. The shaded area represents the region where good mid-IR NLO crystals are expected.

but small energy band gap, so neither of them are not good candidates for mid-IR NLO applications. Instead, the basic units containing chlorine and/or bromine are preferred. Figure 11 displays the distribution of the band gaps and SHG coefficient of the crystals, which exhibits a negative correlation, demonstrating the tendency that a larger energy band gap would result in the smaller NLO effect in crystal. In particular, the yellow area in Fig. 11 indicates the preferred optical range for a good mid-IR crystal with energy band gap larger than 3.0 eV and SHG effect larger than  $10 \times \text{KDP}$ . The crystals  $\text{Cs}_2\text{Hg}_3\text{Cl}_3$ ,  $\text{SbCl}_3, \text{SbBr}_3$ ,  $\text{NaSb}_3\text{Br}_{10}$  and  $\text{HgBr}_2$  are located in this area, and have the potentials for the comprehensive capability of NLO applications in the mid-IR region.

# 4.3. The elucidation of the relationship between dipole moment and SHG effect in molybdenum tellurite crystals

The superposition principle of SHG effect states that the macroscopic SHG coefficients are the geometric superposition of the microscopic second-order susceptibility. This means that the microscopic dipole moments in parallel orientation are beneficial to the favorable superposition of the macroscopic second-order susceptibility. It was widely believed that the NLO responses are determined by the overall dipole moment in crystal. Thus, the explorations of novel NLO crystals have mainly focused on the crystals with polar space group. So far, quite a few polar molybdenum tellurites with large SHG effects have been discovered.<sup>76-</sup>.<sup>80</sup> However, it was

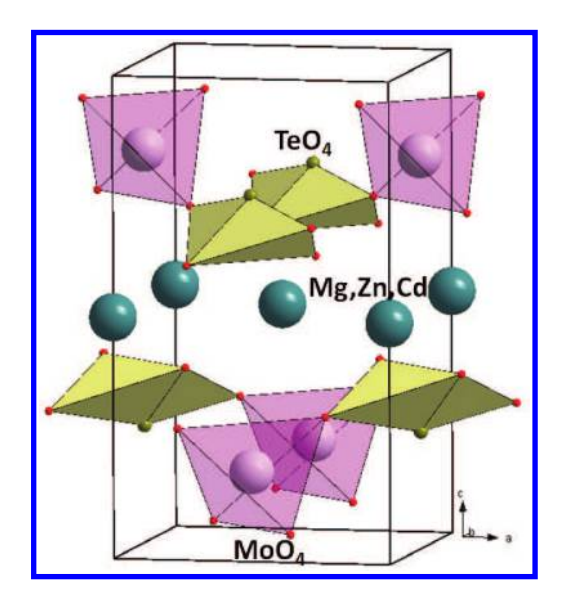


Fig. 12. The unit cell of MgTeMoO<sub>6</sub>, ZnTeMoO<sub>6</sub> and CdTeMO<sub>6</sub>.

also found that a series of non-polar molybdenum tellurite NLO crystals, including MgTeMoO<sub>6</sub> (MTM), CdTeMoO<sub>6</sub> (CdTM), ZnTeMoO<sub>6</sub> (ZnTM-1) (their crystal structures are shown in Fig. 12), possess very large SHG effect, but in those crystals the microscopic dipole moments of respective groups exactly counteract each other and the overall dipole moments are equal to zero. Consequently, it is greatly desirable to perform in-depth investigation on these crystals by first-principles method to elucidate the relationship of the NLO effect and dipole moments.<sup>81</sup>

Table 7 lists the calculated and experimental linear and NLO properties of all NLO molybdenum tellurites, in which except MTM, CdTM and ZTM-1, the others all belong to polar space group. Clearly, the calculated results are consistent with the available experimental results. Interestingly, all the three nonpolar crystals have large SHG effect, even slightly larger than those of their polar counterpart. The atom-cutting analysis for the nonpolar crystals reveals that although the intrinsic microscopic dipole moment of  $(\text{TeO}_4)^{4-}$  square pyramid is much larger than that of  $(\text{MoO}_4)^{2-}$  tetrahedron, the contribution of the former to the SHG coefficients is neglectably small compared with the latter. The results that the crystals (or group) with smaller dipole moment possess the larger SHG effect is contrary to the common belief that the microscopic group with larger second-order susceptibility must have a larger dipole moment.

To elucidate the relationship between the intrinsic dipole moment and SHG effect. We proposed a "flexible dipole model", in which the valence electrons simplified to point charge are bounded between the bonding atoms. A empirical "flexible index" is defined to quantitatively describe the flexibility of the valence bond as

crystals (the below section)							
	$\rm MgTeMoO_6$	${\rm CdTeMoO}_6$	$\rm ZnTeMoO_6$	$\operatorname{ZnTeMoO_6}  \operatorname{Cs_2TeMo_3O_{12}}$	$\rm Zn_2 TeMoO_7$	$\mathrm{Zn_2TeMoO_7}$ $\beta\text{-BaTeMo_2O_9}$	$\rm Na_2 Te_3 Mo_3 O_{16}$
Exp. (KTP) Cal. (KTP)	1.5	2 1.0	1.1	0.5	$0.1 \\ 0.4$	0.7 0.8	0.8 0.6
$\begin{array}{c} \operatorname{MgTM} \\ \mu_z \text{ (Debye)} \\ d_{14} \text{ (pm/V)} \end{array}$	Total 0.00 14.04	Mg-1 0.00 0.06	Mg-2 0.00 0.07	$TeO_{4}-1$ -2.39 -0.19	$TeO_{4}-2$ 2.39 0.11	$MoO_{4}-1$ -0.20 6.76	$MoO_4-2$ 0.20 7.51
CdTM $\mu_z$ (Debye) $d_{14}$ (pm/V)	Total 0.00 11.75	$CdO_{4}-1$ 0.00 -0.55	$CdO_4-2$ 0.00 -0.53	$TeO_{4}-1$ $2.55$ $-0.43$	$TeO_{4-2}$ -2.55 0.14	MoO <sub>4</sub> -1 0.16 6.36	$MoO_{4-2} -0.16$ 5.68
$\frac{\text{ZnTM}}{\mu_z \text{ (Debye)}}$ $\frac{d_{14} \text{ (pm/V)}}{}$	Total 0.00 10.61	Zn-1 0.00 0.07	Zn-2 0.00 0.07	TeO <sub>4</sub> -1 $2.27$ $0.05$	$TeO_{4-2}$ $-2.27$ $-0.15$	$MoO_{4}-1$ $-0.05$ $5.89$	MoO <sub>4</sub> -2 0.05 5.25

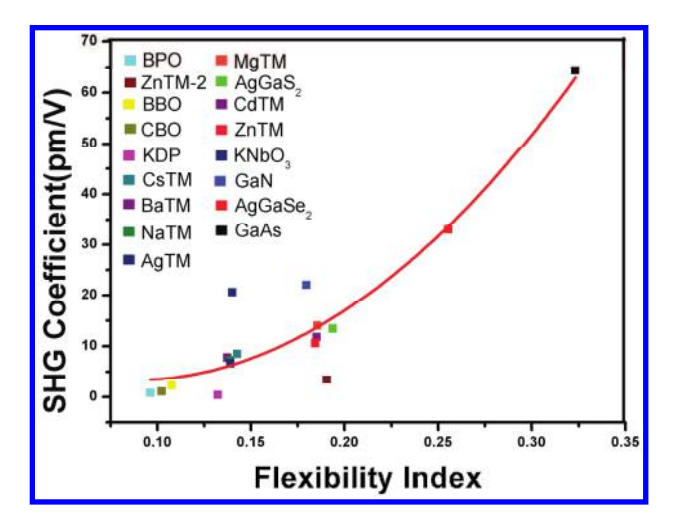


Fig. 13. The dependence of the SHG effect on the flexible index is clear that the SHG effect increases as the flexible index increases.

follows,

$$F = \frac{\exp[(R_0 - R_a)/B]}{(\sqrt{C_a} + \sqrt{C_b})^2 / R_a^2}.$$
 (7)

Here the numerator is the bond valence charge (from the bond valence sum  $model^{82}$ ), where the  $R_a$  is the average bond length of the group which contributes mostly to the SHG effect,  $R_0$  is a tabulated parameter, expressing the ideal bond length between the bonding atoms and B is an empirical constant representing the variation of bond valence with respect to bond length (typically 0.37 Å for the bond connected to oxygen). The denominator is the Coulombic interaction from the atom cores  $(C_a \text{ and } C_b)$  to the bond of the valence electrons. The flexibility index describes the ability to form an induced dipole moment when the electrons are subjected to the external perturbation. Figure 13 plots the dependence of the largest SHG coefficient on the flexibility index in the various types and it is clear that the SHG coefficients and the flexibility index are positively correlated. It should be noted that the flexibility index is independent of the intrinsic dipole moment and only the induced dipole moments are considered. Therefore, the results from the "flexible dipole model" demonstrate that the induced dipole moments oscillated by the external field, rather than the intrinsic dipole moments, determine the NLO response.

### 5. Conclusions and Outlook

The search for new NLO crystals, particularly in the UV and IR spectral regions, is still very active, even though intensive efforts in this field have been in progress for more than 50 years. The first-principles studies by DFT method have the capability to accurately predict the optical properties in NLO crystals, i.e., energy band

gaps, refractive indices, birefringence and SHG coefficients, without any experimental parameter. With the ab initio computational method, the researchers can judge if the synthesized materials are suitable for the practical NLO applications just at the very initial stage of materials discovery. Moreover, the developments of DFT analysis tools make it possible to deeply understand the intrinsic mechanism of optical properties in crystals at the microscopic atomic scale. The thorough elucidation of the structure-property relationship between NLO effects and microstructure are extremely important for the exploration of new NLO crystals with superior performances in high efficiency. It should be emphasized that, apart from the research topics presented in this review, the DFT methods have also been used to investigate other scientific issues in the NLO crystal fields, e.g., to elucidate the influence of impurities and defects on the optical properties<sup>83</sup> and to analyze the Raman spectrum in the crystal-growth process.<sup>84</sup> In fact, besides the NLO crystals, many material fields such as photocatalysts and nano-materials also greatly benefit from the DFT studies. $^{85-87}$  We believe that with the optimization of the computational algorithms and the acceleration of supercomputer speeds, the first-principles research approaches will play a more and more important role in the exploits of many advanced functional materials.

## Acknowledgments

This work was supported by the National Natural Science Foundation of China under Grant Nos 11174297 and 11474292, and the National Basic Research Project of China (No 2011CB922204), and Foundation of the Director of Technical Institute of Physics and Chemistry, CAS. MHL thanks NCHC(TW) for database service and KeyWin Elec. Inc. for equipment donation.

## References

- 1. T. H. Maiman, Nature 187, 493 (1960).
- 2. P. A. Franken et al., Phys. Rev. Lett. 7, 118 (1961).
- 3. T. Brabec and F. Krausz, Rev. Mod. Phys. 72, 545 (2000).
- 4. X. Lin, G. Zhang and N. Ye, Cryst. Growth Des. 9, 1186 (2009).
- 5. G. Zhang et al., Appl. Phys. Lett. 95, 261104 (2009).
- T. K. Bera et al., J. Am. Chem. Soc. 132, 3484 (2010).
- 7. S. Wang et al., J. Am. Chem. Soc. 132, 8779 (2010).
- 8. H. Huang et al., J. Am. Chem. Soc. 135, 18319 (2013).
- 9. H. Huang et al., Angew. Chem. Int. Ed. **50**, 9141 (2011).
- 10. S. C. Wang and N. Ye, J. Am. Chem. Soc. 133, 11458 (2011).
- 11. G. Zou et al., J. Am. Chem. Soc. 133, 20001 (2011).
- 12. G. Zhang et al., J. Am. Chem. Soc. 134, 14818 (2012).
- 13. C. T. Chen et al., Adv. Mater. 11, 1071 (1999).
- 14. L. Kang et al., J. Mater. Chem. C 1, 7363 (2013).
- 15. R. C. Miller, Appl. Phys. Lett. 5, 17 (1964).
- 16. Bloembergen, Nonlinear Optics (Benjamin, New York, 1965), p. 5.
- 17. C. R. Jeggo and G. D. Boyd, J. Appl. Phys. 41, 2741 (1970).

- 18. B. F. Levine, Phys. Rev. Lett. 25, 440 (1970).
- 19. C. Chen, Z. Lin and Z. Wang, Appl. Phys. B-Lasers Opt. 80, 1 (2005).
- 20. Z. S. Lin et al., J. Phys. D-Appl. Phys. 47, 253001 (2014).
- 21. W. Kohn, Rev. Mod. Phys. 71, 1253 (1999).
- 22. M. Elstner et al., Phys. Rev. B 58, 7260 (1998).
- 23. D. J. Tozer et al., Mol. Phys. 97, 859 (1999).
- 24. D. M. Ceperley and B. J. Alder, Phys. Rev. Lett. 45, 566 (1980).
- 25. J. P. Perdew, K. Burke and M. Ernzerhof, Phys. Rev. Lett. 78, 1396 (1997).
- 26. A. Seidl et al., Phys. Rev. B 53, 3764 (1996).
- 27. A. D. Becke, J. Chem. Phys. 98, 5648 (1993).
- 28. M. Ernzerhof and G. E. Scuseria, J. Chem. Phys. 110, 5029 (1999).
- 29. Z. S. Lin et al., Comput. Chem. Sci. 60, 99 (2012).
- 30. S. J. Clark et al., Z. Kristallogr. 220, 567 (2005).
- 31. M.-H. Lee et al., Psi\_k Newsletters 67 (February) Highlights, 145 (2005).
- 32. A. M. Rappe et al., Phys. Rev. B 41, 1227 (1990).
- 33. J. S. Lin et al., Phys. Rev. B 47, 4174 (1993).
- 34. L. Kleinman and D. M. Bylander, Phys. Rev. Lett. 48, 1425 (1982).
- 35. H. J. Monkhorst and J. D. Pack, Phys. Rev. B 13, 5188 (1976).
- E. D. Palik, Handbook of Optical Constants of Solids (Academic Press, New York, 1985).
- 37. S. N. Rashkeev, W. R. L. Lambrecht and B. Segall, Phys. Rev. B 57, 3905 (1998).
- 38. J. Lin et al., Phys. Rev. B 60, 13380 (1999).
- 39. R. He et al., J. Appl. Phys. 109, 103510 (2011).
- 40. C.-H. Lo, Master's Degree thesis, Tamkang University (2005).
- 41. M.-H. Lee *et al.*, Analysing calculated nonlinear optical properties with a weighted-density scheme: The mechanism of second-harmonic generation in oxides and the role of oxygen lone-pair electrons, in preparation.
- 42. M. H. Lee, C. H. Yang and J. H. Jan, Phys. Rev. B 70, 235110 (2004).
- 43. Z. S. Lin et al., Phys. Rev. B 62, 1757 (2000).
- 44. L. Kang et al., J. Phys.-Condens. Matter 24, 335503 (2012).
- 45. Z. S. Lin et al., J. Appl. Phys. 93, 9717 (2003).
- 46. Z. S. Lin et al., J. Appl. Phys. 90, 5585 (2001).
- 47. H. Huang et al., J. Appl. Phys. 106, 0.3107 (2009).
- 48. G. D. Boyd et al., Appl. Phys. Lett. 5, 234 (1964).
- 49. H. A. Lu et al., Appl. Phys. Lett. 62, 1314 (1993).
- 50. R. C. Eckardt et al., IEEE J. Quantum Electron. 26, 922 (1990).
- 51. J. E. Hesse et al., Proc. Nat. Aca. Sci. 81, 4746 (1984).
- 52. L. A. Laimins, D. B. Rhoads and W. Epstein, Proc. Nat. Aca. Sci. 78, 464 (1981).
- 53. E. H. Lieb, Phys. Rev. Lett. 19, 108 (1967).
- 54. Y. G. Hao, X. Y. Sun and N. S. Dalal, Ferroelectrics 132, 165 (1992).
- 55. B. Silvi, Z. Latajka and H. Ratajczak, Ferroelectrics 150, 303 (1993).
- 56. Z. S. Lin et al., J. Chem. Phys. 118, 2349 (2003).
- 57. G. H. Zou et al., J. Am. Chem. Soc. 135, 18560 (2013).
- 58. M. Luo et al., Crystengcomm 16, 4414 (2014).
- 59. M. Luo et al., Inorg. Chem. 53, 8098 (2014).
- 60. L. Kang et al., J. Phys. Chem. C 117, 25684 (2013).
- 61. L. Kang et al., Sci. Rep. 3, 1366 (2013).
- 62. L. Bai et al., J. Appl. Phys. 103, 188772 (2008).
- 63. L. Bai et al., J. Chem. Phys. 120, 8772 (2004).
- 64. J. Yao et al., Inorg. Chem. 49, 9212 (2010).

- 65. D. Mei et al., Dalton Trans. 40, 3610 (2011).
- 66. K. Feng et al., Dalton Trans. 42, 13635 (2013).
- 67. K. Feng et al., J. Mater. Chem. C 2, 4590 (2014).
- G. D. Boyd, H. Kasper and J. H. McFee, IEEE J. Quantum Electron. QE 7, 563 (1971).
- 69. G. D. Boyd, E. Buehler and F. G. Storz, Appl. Phys. Lett. 18, 301 (1971).
- 70. V. Petrov et al., Appl. Phys. B-Lasers Opt. 78, 543 (2004).
- 71. Q. Wu et al., Dalton Trans. 2014(43), 8899 (2014).
- 72. Q. Wu et al., Inorg. Chem. Commun. 34, 1 (2013).
- 73. Q. Wu et al., J. Am. Chem. Soc. 136, 5683 (2014).
- 74. Y. Dang et al., Dalton Trans. 2013(42), 9893 (2013).
- 75. S. Lv et al., J. Mater. Chem. C 2, 6796 (2014).
- 76. Y. Zhou et al., Dalton Trans. 2009(29), 5747 (2009).
- 77. H. S. Ra, K. M. Ok and P. S. Halasyamani, J. Am. Chem. Soc. 125, 7764 (2003).
- 78. J. Zhang et al., Cryst. Growth Des. 11, 1863 (2011).
- 79. W. Zhang et al., Crystengcomm 14, 3490 (2012).
- 80. N. Sau Doan, S.-H. Kim and P. S. Halasyamani, Inorg. Chem. 50, 5215 (2011).
- 81. X. Jiang et al., J. Mater. Chem. C 2, 530 (2014).
- 82. I. D. Brown, The Chemical Bond in Inorganic Chemistry: The Bond Valence Model (Oxford University Press, 2002).
- 83. Z. S. Lin et al., Phys. Rev. B 82, 035124 (2010).
- 84. S. Liu et al., J. Appl. Crystallogr. 47, 739 (2014).
- 85. Z. Zhao and Q. Liu, Catal. Lett. 124, 111 (2008).
- 86. S. Laursen and S. Linic, PCCP 11, 11006 (2009).
- S. Ogata, Y. Umeno and M. Kohyama, *Modell. Simul. Mater. Sci. Eng.* 17, 013001 (2009).